

Molecular transport through 3-hydroxybutyrate co-3-hydroxyhexanoate biopolymer films with dispersed graphene oxide nanoparticles: Gas barrier, structural and mechanical properties

H. Mahmood^{a,b}, A. Pegoretti^{a,b}, Roberto S. Brusa^{c,d}, R. Ceccato^a, L. Penasa^{c,d}, S. Tarter^c, R. Checchetto^{c,*}

^a Department of Industrial Engineering, University of Trento, Via Sommarive 9, I-38123, Trento, Italy

^b National Interuniversity Consortium of Materials Science and Technology (INSTM), Via Giuseppe Giusti 9, I-50121, Florence, Italy

^c Department of Physics, University of Trento, Via Sommarive 14, I-38123, Trento, Italy

^d TIFPA/INFN, Via Sommarive 14, I-38123, Trento, Italy

ARTICLE INFO

Keywords:

Biopolymer nanocomposites
Molecular diffusion
Free volume structure
Gas barrier properties
Mechanical properties

ABSTRACT

Poly(3-hydroxybutyrate-co-3-hydroxyhexanoate) (PHBH) nanocomposite films containing 0.25 wt % of Graphene Oxide (GO) nanoparticles were prepared by solution-casting and characterized by Differential Scanning Calorimetry (DSC), X-Rays Diffraction (XRD) and Positron Annihilation Lifetime Spectroscopy (PALS). Gas transport properties were analyzed in the 295–343 K interval using CO₂, N₂, D₂ and He. Neat PHBH films showed a semi-crystalline structure with lamellar crystalline domains of 30 ± 1 and 5 ± 1 nm size in the (020) and (002) direction, respectively. GO dispersion increases the PHBH crystalline fraction from 0.28 to 0.60 wt. % without changing the size of crystalline domains and the structure of the PHBH free volume. Nanocomposite films show mechanical properties similar to those of the neat PHBH film but improved gas barrier properties as consequence of the larger number density of the gas-impermeable crystalline domains.

1. Introduction

Poly(3-hydroxybutyrate) (PHB) is a biodegradable and biocompatible semi-crystalline polyester produced by microorganisms in specific fermentation conditions from sugar and lipids and act as intercellular-carbon and energy-storage compound [1]. It is based on 3-hydroxybutyric acid (C₄H₈O₃), has glass transition temperature $T_g \sim 4^\circ\text{C}$, melting temperature $T_m \sim 180^\circ\text{C}$, a crystalline degree of 60 ± 5% and tensile strength similar to that of polypropylene (PP) [1,2]. Its possible applications in different technologies, as a substitute of commercial petroleum-derived commercial polymers, are impeded by some shortcomings. In particular, the main limitation is its elevated brittleness which is a consequence of its high crystallinity and its low resistance to thermal degradation which, owing to the high T_m value, leads to a narrow range of processing temperature [3–5]. Poly(3-hydroxybutyrate-co-3-hydroxyhexanoate) (PHBH) is a biodegradable PHB copolymer developed to mitigate the PHB drawbacks: it can be obtained either by microorganisms or chemical synthesis and consists of

randomly arranged 3-hydroxybutyrate units (3HB: [-O-CH-(CH₃)-CH₂-C(=O)-]_n) and 3-hydroxyhexanoate (3HH: [-O-CH-(C₃H₇)-CH₂-C(=O)-]_n) units [6]. Structurally, 3HH units are excluded from the 3HB lattice and thus form short branches which reduce the regularity of the PHBH molecular chains arrangement and thus the crystalline fraction. Compared to PHB, the addition of the 3HH units broadens the processing temperature range and increases the ductility but decreases the storage modulus and the strength [7,8]. This biopolymer is expected to find applications in different technologies as, for example, in the construction of automotive interior components or of electrical devices [9]. Therefore most literature studies are aimed to improve the PHBH mechanical properties by, for example, varying the 3HH fraction in the PHBH matrix [3,4], by the addition of filler nanoparticles such as cellulose nano-crystals [10,11] or glass fibers [12].

This paper is dedicated to the study of neat PHBH films and of PHBH nanocomposite films containing 0.25 wt % of graphene oxide (GO) nanoparticles (GO-PHBH, in the following). We studied the gas transport and mechanical properties of pure and nanocomposite film samples and

* Corresponding author.

E-mail addresses: haroon.mahmood@unitn.it (H. Mahmood), alessandro.pegoretti@unitn.it (A. Pegoretti), robertosennen.brusa@unitn.it (R.S. Brusa), riccardo.ceccato@unitn.it (R. Ceccato), luca.penasa@unitn.it (L. Penasa), stefania.tarter@studenti.unitn.it (S. Tarter), riccardo.checchetto@unitn.it (R. Checchetto).

<https://doi.org/10.1016/j.polymeresting.2019.106181>

Received 8 July 2019; Received in revised form 27 September 2019; Accepted 19 October 2019

Available online 21 October 2019

0142-9418/© 2019 Elsevier Ltd. All rights reserved.

correlated the observed results to the structural information obtained by different characterization techniques such as X-Rays Diffraction (XRD), Differential Scanning Calorimetry (DSC), Thermogravimetric Analysis (TGA) and Positron Annihilation Lifetime Spectroscopy (PALS).

Graphene-derived nanoparticles are effective fillers for improving the mechanical properties of polymer films and reducing the transport rates of penetrant molecules [13,14]. PHBH nanocomposites containing this high aspect ratio filler nanoparticle can find applications in modified atmosphere packaging as gas barrier for CO₂ (bacterial and fungal growth inhibitor) and N₂ (inert gas used as alternative to vacuum) [15–18], in the construction industry as protective layer against the permeation of gases [19,20], in the oil and gas industry [21,22] and in modern high-voltage apparatuses [23] to impede the permeation of the corrosive CO₂ gas.

2. Experimental section

Nanocomposites preparation. The materials used in this work are: i) biodegradable PHBH (3-hydroxybutyrate co-3-hydroxyhexanoate) provided by Kaneka Co. LTD, Osaka, Japan (density $\rho = 1.19 \text{ g/cm}^3$, melting temperature $T_m = 126 \text{ }^\circ\text{C}$), ii) water suspension of Graphene Oxide (GO) provided by Graphenea, Spain (4 mg/ml GO concentration, pH value = $2.2 \div 2.5$, GO monolayer content > 95%, GO size < 10 μm). GO-PHBH nanocomposites were prepared by the following procedure. 0.25 mg PHBH were dissolved in 25 ml dimethylformamide [DMF: (CH₃)₂NC(O)H] solvent in a beaker under magnetic stirring. Subsequently, 0.156 ml of GO suspension was added to the PHBH/DMF solution which was then stirred for at least 1 h at 80 $^\circ\text{C}$. Film with thickness of about 70 μm were then prepared by solution-casting by pouring the prepared solution in a Petri dish and drying it in an oven under ambient pressure for 15 h at 80 $^\circ\text{C}$. The sample mass density was measured by Archimedes method: obtained values were 1.14 ± 0.01 and $1.18 \pm 0.01 \text{ g/cm}^3$ for the neat PHBH and nanocomposite GO-PHBH sample, respectively. With the above described procedure for nanocomposite preparation, it was observed that GO contents larger than 0.25 wt % disrupted the PHBH matrix and produced very brittle samples, reasonably consequence of the filler agglomeration. At this low filler content, no evidence of filler agglomeration was found analyzing the nanocomposite cross-section by high resolution Scanning Electron Microscopy (SEM).

Structural analysis. XRD spectra were collected by means of a Rigaku D-MAX IIIID powder diffractometer in Bragg-Brentano geometry, using CuK α monochromatic radiation ($\lambda = 0.154056 \text{ nm}$) and a graphite monochromator in the diffracted beam. Spectra were acquired in symmetric scattering configuration in the 5 $^\circ$ –80 $^\circ$ 2 θ range at 0.05 $^\circ$ sampling interval with 4 s counting time. Jade 8 $\text{\textcircled{R}}$ software (MDI Corp. USA) was employed for the peak refinement and peak parameter evaluation. The crystallite dimensions, along different directions, were determined by using the Scherrer equation.

Thermal analysis. Thermogravimetric analysis (TGA) was performed using a Mettler TGA Q5000 instrument at a heating rate of 10 $^\circ\text{C}/\text{min}$ between 30 and 700 $^\circ\text{C}$ under a nitrogen flow of 100 ml/min. Differential Scanning calorimetry (DSC) analysis was carried out using a Mettler DSC 30 calorimeter using approximately 10 mg sample by the following procedure. The test was carried out under a constant nitrogen flow of 100 ml/min in which a cyclic heating-cooling-heating analysis was performed between –30 $^\circ\text{C}$ and 200 $^\circ\text{C}$ at a rate of 10 $^\circ\text{C}/\text{min}$.

Mechanical tests. Tensile tests were performed on thin films of pure PHBH and GO-PHBH specimen strips having dimensions of 20 mm \times 5 mm which were tested at 0.1 mm/min until break using DMA Q800 dynamic mechanical analyzer (TA instruments Co. LTD) at room temperature. Moreover, by using the same apparatus, the viscoelastic properties of the neat PHBH and GO-PHBH nanocomposites were investigated at 1 Hz frequency on samples having dimensions of 45 mm \times 5 mm \times 2 mm in the temperature range from 0 to 100 $^\circ\text{C}$ with heating ramp of 3 $^\circ\text{C}/\text{min}$.

Positron Annihilation Lifetime Spectroscopy (PALS) measurement. PALS analysis was carried out with a fast-fast coincidence apparatus [24]. The detectors were two BaF₂ scintillators coupled to Hamamatsu H3378 photomultiplier tubes. The Na²² positron source sandwiched between two identical samples was placed between the two detectors. The start signal was given by the 1274 keV line emitted by the Na²² [22] source simultaneously to the emission of a positron. The stop signal was given by the 511 keV line due to the positron and positronium pick-off annihilation in the sample. The signal from the detectors are sent to two ORTEC 583B constant fraction differential discriminators (CFDD). The two lines, with a delay in the stop branch, were connected to an ORTEC 566 time to amplitude converter (TAC) and its output to a FASTComTec multichannel analyzer (MCA4). The time resolution measured by using a Co-60 source was found to be 260 ps. PALS lifetime spectra were analyzed using LT9 package [25].

Gas transport tests. Gas transport was studied by gas phase permeation technique using membrane samples shaped as thin disc with diameter $d \sim 1 \text{ cm}$ and thickness $h \sim 70 \mu\text{m}$. At time $t = 0$ one side of the membrane (*HPS*: high pressure side) was exposed to the test gas kept at constant pressure p_{HPS} while the opposite side (*LPS*: Low Pressure Side) faced a vacuum chamber with background pressure $\sim 10^{-7} \text{ Pa}$. Gas molecules were absorbed in the *HPS* layers of the membrane ($x = 0$), diffused through the membrane layers down to their concentration gradient, reached the *LPS* of the membrane ($x = l$) and permeated in the UHV chamber. Here desorbed molecules formed a rarefied gas with partial pressure $p_{LPS}(t)$ which was measured by a calibrated Quadrupole Mass Spectrometer (QMS). The QMS ion current $I_m(t)$ pertinent to the permeating test gas was recorded as a function of time t and provided the $p_{LPS}(t)$ value according to the relation $p_{LPS}(t) = I_m(t)/\alpha$ where α is the QMS sensibility for the test gas. In our experimental approach the vacuum chamber was continuously pumped and the gas permeation flux $j_m(t)$ was thus evaluated by the relation $S_p[p_{LPS}^{sign}(t) - p_{LPS}^{back}] = Aj_m(t)$ where $A = \frac{1}{4}\pi d^2$ is the membrane surface area, S_p the pumping speed of the vacuum system and p_{LPS}^{back} the background partial pressure of the permeating gas [26]. In the present experimental approach, the average value of the p_{LPS}^{back} fluctuations, δp_{LPS}^{back} , defines the flux detection limit $\delta j_m = \frac{1}{A} S_p \delta p_{LPS}^{back}$. The gas transport process was studied using penetrant molecules with different size and condensation properties, as described by their kinetic diameters (σ_k) and critical temperature T_c : deuterium (²H₂: $\sigma_k = 0.29 \text{ nm}$, $T_c = 38.2 \text{ K}$), helium (He: $\sigma_k = 0.26 \text{ nm}$, $T_c = 5.2 \text{ K}$), carbon dioxide (CO₂: $\sigma_k = 0.33 \text{ nm}$, $T_c = 304 \text{ K}$) and nitrogen (N₂: $\sigma_k = 0.36 \text{ nm}$, $T_c = 126.2 \text{ K}$) [26]. With the experimental set-up used for the present permeation tests δj_m was $\sim 1 \times 10^{-5} \text{ mL(STP) m}^{-2} \text{ s}^{-1}$ for N₂ and CO₂ and $\sim 1 \times 10^{-6} \text{ mL(STP) m}^{-2} \text{ s}^{-1}$ for D₂ and He. Details on the experimental apparatus and procedures are presented in previously published papers [27,28].

3. Results and discussion

In Fig. 1, TGA thermograms of the neat and GO-PHBH nanocomposite are presented. It can be observed that the onset temperature T_{on} of the decomposition process increases from 231 $^\circ\text{C}$ for neat PHBH to 258 $^\circ\text{C}$ for the GO-PHBH nanocomposite with 0.25 wt % filler content. This could be attributed to the presence of GO flakes forming a barrier to the escape of the volatile products. Therefore the addition of the GO filler particles slightly improves the thermal stability of the PHBH matrix.

The first DSC heating scan of pure PHBH and GO-PHBH nanocomposite samples is shown in the upper panel of Fig. 2. It can be observed that spectra exhibit two endothermic peaks at $T_{m1} = 135 \pm 1 \text{ }^\circ\text{C}$ and $T_{m2} = 146 \pm 1 \text{ }^\circ\text{C}$. The peak at T_{m1} is due to melting of the PHBH nanocrystals formed at room temperature after synthesis while the peak at T_{m2} is due to the melting of the nanocrystals formed during the heating stage of the DSC test [29]. The overall melting enthalpy $\Delta H_m = \Delta H_{T_{m1}} + \Delta H_{T_{m2}}$ increases with the GO addition from -

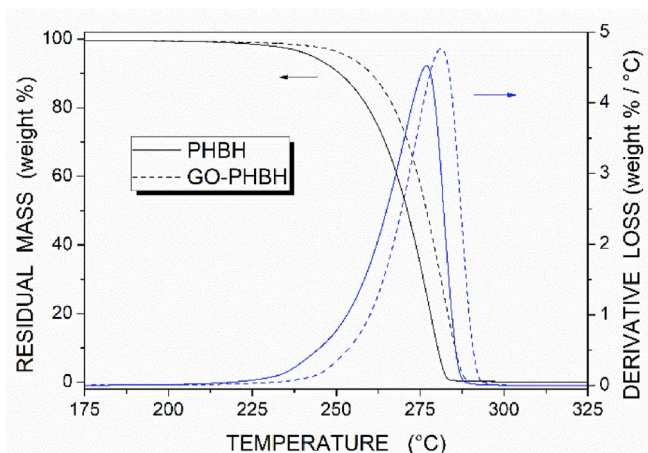


Fig. 1. TGA thermograms (left y-scale) and derivative weight loss (right y-scale) of the neat PHBH and nanocomposite GO-PHBH films.

60.6 J/g for the pure PHBH matrix to -108.4 J/g for the nanocomposite with 0.25 wt % filler content. The crystalline fraction x_c of as-prepared samples was evaluated by the relation $x_c = \frac{\Delta H_{T_{m1}}}{\Delta H_m^0(1-\phi)}$ where ϕ is the filler weight fraction, $\Delta H_{T_{m1}}$ the enthalpy value related to the melting peak at T_{m1} and $\Delta H_m^0 = 146$ J/g is the melting enthalpy of 100% crystalline PHBH [30]. The $\Delta H_{T_{m1}}$ term was evaluated considering the DSC signal 90 °C and 170 °C, subtracting the baseline and fitting the two peaks using Origin® software: we found that the first melting peak lies between 96 °C and 140 °C both in the neat and nanocomposite sample. The as-prepared PHBH film exhibited a crystalline fraction $x_c^{PHBH} = 0.28$ while after the GO addition the crystalline fraction increased to $x_c^{GO-PHBH} = 0.60$.

The central panel of Fig. 2 reports the cooling curves of the PHBH and GO-PHBH samples. In the cooling scan of the GO-PHBH nanocomposite we can observe an exothermic peak at $T_c \sim 60$ °C revealing the formation of PHBH crystals. The presence of crystallization peak in the GO-PHBH scan indicates that GO filler particles promoted the PHBH crystallization hence acting as nucleation centers for PHBH crystals. This peak is not observed in the cooling scan of the neat PHBH sample because the GO preferential nucleation centers are not present and because the cooling rate was fast enough to prevent the crystallization process.

Cold-crystallization of the neat PHBH film occurred at $T_c \sim 56$ °C, as it can be seen in the lower panel of Fig. 2: DSC spectra obtained in the second heating scan exhibit a similar melting peak structure as in the first scan (in the 125–150 °C temperature interval) but at lower T_{m1} values.

The PHBH crystalline fraction after cold crystallization at $T_c \sim 60$ °C, \hat{x}_c was evaluated by the relation $\hat{x}_c = \frac{\Delta H_m}{\Delta H_m^0(1-\phi)}$ where ϕ is the filler weight fraction. The obtained values are reported in Table 1. The semi-crystalline state of the pure and nanocomposite samples is due to their casting process which involved, in fact, a long duration drying step at $T = 80$ °C which is higher than T_c .

The increased PHBH crystalline fraction after GO addition, from 0.28 to 0.60, is accompanied by a 3% increase of the density, from 1.14 ± 0.01 to 1.18 ± 0.01 g/cm³ suggesting that in the present samples the mass density of the PHBH crystallite is only $\sim 5\%$ larger than that of the amorphous PHBH material.

The XRD spectra of the neat PHBH film and of the GO-PHBH nanocomposite film are reported in Fig. 3. The pattern can be attributed to a semi-crystalline material, with the presence of the orthorhombic structure of poly(3-hydroxybutyrate), in the α -form [30]. The following peaks can be recognized and attributed to the specific (hkl) family of planes: (020) at 13.7°, (110) at 17.1°, (021) at 20.3°, (101) at 21.6° and (002) at

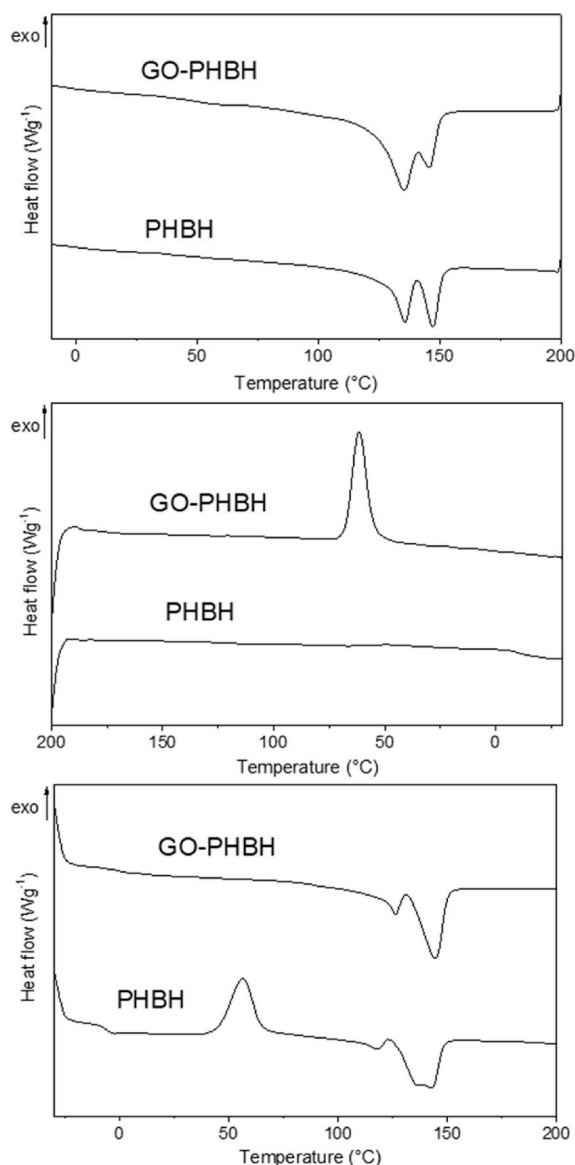


Fig. 2. DSC scans of the neat PHBH and of the GO-PHBH nanocomposite films. Upper panel: first heating. Central panel: first cooling. Lower panel: second heating.

Table 1
Thermodynamic parameters obtained from DSC analysis.

	T_{m1}	T_{m2}	ΔH_{m1}	ΔH_m	x_c	\hat{x}_c	T_c
PHBH	136 °C	147 °C	-41.2 J/g	-60.6 J/g	0.28	0.41	56 °C
GO-PHBH	135 °C	146 °C	-87.8 J/g	-108.4 J/g	0.60	0.74	62 °C

30.35°. It is possible to note that the intensity of the peaks and bands laying in the range 20°–35° was larger than that of spectra reported in the literature for neat PHB and PHBH films [31,32]. This evidence suggests that the biopolymer crystallization occurring at low temperature during the sample preparation, leads to a more complex tridimensional geometry of the PHBH crystallites.

A feature resulting from the comparison of the spectra of PHBH and GO-PHBH samples is the shift towards slightly larger d -values of all peaks at $2\theta < 25^\circ$ in nanocomposite one. The shift of the (020) peak, for example, indicates that the d -values increases from 0.644 nm in PHBH to

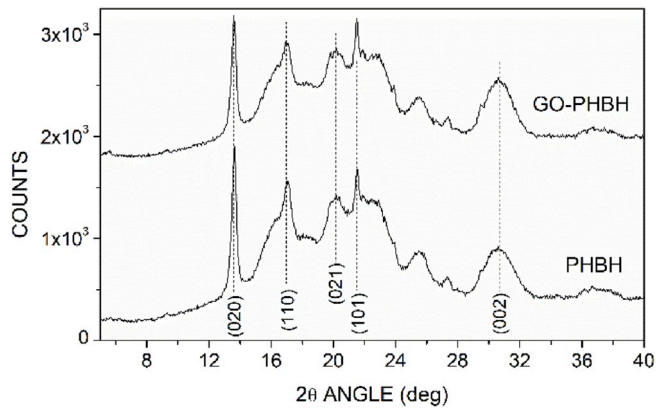


Fig. 3. XRD spectra of the neat PHBH film and of the nanocomposite GO-PHBH film.

0.650 nm in GO-PHBH, while the shift of the (110) peak indicates that the d -values increases from 0.558 nm in PHBH to 0.563 nm in the nanocomposite. This small increase suggested that the GO filler particles, where the PHBH crystallites preferentially nucleates, intercalate into the polymer chains.

The Scherrer equation has been used in order to evaluate crystallite size along two different directions with the aim to quantify the anisotropy of the crystalline domains. To evaluate the lamellar thickness for b -axis direction the (020) peak at 13.7° was analyzed whereas for c -axis the (002) peak at 30.35° was selected [32]. The following values were obtained: 30 ± 1 nm for (020) and 5 ± 1 nm for (002). The latter value resulted to be very close to that reported for neat PHBH films, at low crystallization temperature which was lower than the values obtained for co-polymerised PHBH samples [33]. The addition of GO does not alter significantly the microstructure of the films. Specifically, the relative intensities of the two more intense peaks, (020) at 13.7° and (101) at 21.6° , suggests a difference between the crystalline to amorphous ratio in the nanocomposite samples with respect to the ration of the pure one thus confirming the calorimetric information obtained from DSC analysis. Moreover, the Scherrer analysis of the pertinent XRD spectrum, see Fig. 3, indicates that the crystallite size along c direction did not change with filler addition, 5 ± 1 nm, whereas slightly increased in the b direction to 36 ± 1 nm.

For each sample (neat PHBH and GO-PHBH) four lifetime PALS spectra were measured. All spectra were well fitted by the sum of three exponential decay functions: $F(t) = \sum_{j=1}^3 I_j e^{-t/\tau_j}$. The presented three lifetime values τ_j and their intensities I_j are the weighted values of the four measurements. An example of spectrum and its deconvolution in three lifetime is shown in the upper panel of Fig. 4. For neat PHBH samples we obtain: i) a short lifetime value $\tau_1 = 0.223 \pm 0.002$ ns with intensity $I_1 = 32.7 \pm 0.1\%$ attributable to free positron and para-Positronium (p -Ps) annihilation, ii) an intermediate lifetime value $\tau_2 = 0.476 \pm 0.004$ ns with intensity $I_2 \sim 45.1 \pm 0.1\%$ attributable to positron annihilation with oxygen atoms and/or small cavities and iii) a longer lifetime with $\bar{\tau}_3 = 2.108 \pm 0.009$ ns and intensity $I_3 \sim 21.4 \pm 0.1\%$ due to ortho-Positronium (o -Ps) annihilation in nanometer-sized regions of lower electron density, such as voids or free volume cavities [34]. The fitting procedure also provides the distribution function $F(\tau_3)$ of the τ_3 values, see the lower panel of Fig. 4, which is described by a log-norm function having $\sigma = 0.17 \pm 0.03$ ns. [25].

The o -Ps annihilation process is of interest because the τ_3 value can be related to the size of cavities where o -Ps annihilates by the Tao–Eldrup equation

$$\tau_3 = \frac{1}{2} \left(1 - \frac{r}{r + \Delta r} + \frac{1}{2\pi} \sin \left(2\pi \frac{r}{r + \Delta r} \right) \right)^{-1} \quad (1)$$

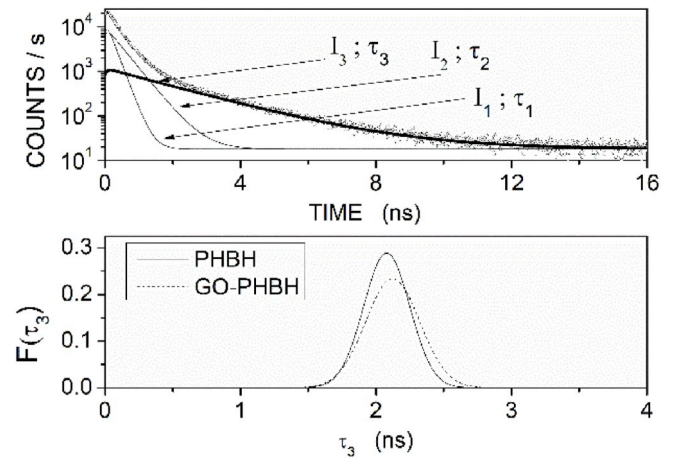


Fig. 4. Upper Panel: PALS spectrum of the neat PHBH film. The fitting exponential decays functions $I_j e^{-t/\tau_j}$ are reported as solid lines while (thick line: o -Ps annihilation signal, $\frac{4}{3}\pi r^3 I_3$ [35,36]). Lower Panel: τ_3 distribution function $F(\tau_3)$ of the neat PHBH and of the nanocomposite GO-PHBH films.

where $\Delta r = 0.166$ nm accounts for the electron shell extending into the free-volume cavity when spherical cavities of radius r are considered; the polymer fractional free volume f_v is proportional to the o -Ps annihilation signal, $\frac{4}{3}\pi r^3 I_3$ [35,36]. In the neat PHBH film the $\bar{\tau}_3 = 2.108 \pm 0.009$ ns value provides the average value of the cavity radius $r_c = 0.29 \pm 0.01$ nm. The interval value of cavity radius r was evaluated by the $F(\tau_3)$ function considering the τ_3 left and right values pertinent to $F(\tau_3)$ at its 10% peak values, $\tau_3 = 1.741$ ns and $\tau_3 = 2.437$ ns, respectively. By the Tau-Eldrup equation we evaluate a cavity radius r with values distributed between 0.26 ± 0.01 nm and 0.32 ± 0.01 nm.

The PALS spectrum pertinent to the GO-PHBH nanocomposite was fitted with $\tau_1 = 0.231 \pm 0.003$ ns ($I_1 \sim 38.8 \pm 0.1\%$), $\tau_2 = 0.471 \pm 0.007$ ns ($I_2 \sim 41.3 \pm 0.1\%$), $\bar{\tau}_3 = 2.163 \pm 0.007$ ns ($I_3 \sim 19.8 \pm 0.1\%$) and $\sigma = 0.20 \pm 0.04$ ns. The analysis of the $F(\tau_3)$ function indicates that the average cavity radius in the GO-PHBH nanocomposite is $r_c = 0.30 \pm 0.01$ nm and that the cavity radius is distributed between 0.26 ± 0.01 nm and 0.33 ± 0.01 nm.

Small variations in the τ_3 distribution functions of the neat and nanocomposite samples results from cavities at the interface between PHBH matrix and the GO filler particles. PALS results indicate that the GO addition does not introduce further positron annihilation channels and gives rise to negligible variations of the free volume structure of the PHBH matrix. Note that the intensity of the I_3 signal is the same, inside the experimental indetermination, in the neat and nanocomposite sample even if the crystalline fraction of the nanocomposite is a factor 2 larger, see Table 1. This can be explained considering the small dimensions of the crystallites and their ordered structure: positrons that thermalize inside the PHBH crystallite diffuse to their interface with the amorphous phase and annihilate there. As a consequence positrons probe with the same intensity the open volume of the amorphous region both in the neat and composite samples.

Mechanical properties. Tensile stress and strain at break of neat PHBH and GO-PHBH casted thin films are shown in Fig. 5. The neat PHBH films presents tensile strength value of about 17 MPa and a strain at break of about 5%. The tensile strength value is larger than that reported by Zhou et al. [10] and by Hosoda et al. [37] for pure PHBH film prepared by cast-film method and comparable with the value obtained by Doi et al. in neat PHBH film [3]. It can be seen that the addition of GO filler in PHBH resulted in a slight lowering of the tensile strength to ~ 14 MPa and strain at break to $\sim 3.5\%$. The decrease of this last parameter reasonably results from the interrupted continuity of the PHBH matrix after filler addition rather than from an incomplete chemical compatibility between filler particles and polymer matrix. An

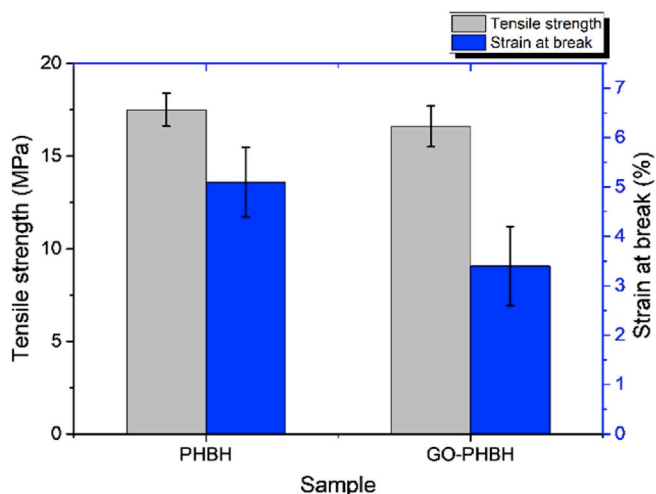


Fig. 5. Tensile strength and strain at break of neat PHBH and nanocomposite GO-PHBH films.

incomplete compatibility would give rise, in fact, to de-wetting effects with formation of supplementary free volumes (voids) at the filler-matrix interface [38–40]: Fig. 4 shows, on the contrary, that only minor changes in the $F(\tau_3)$ function occur after filler dispersion.

The addition of 2.3 wt % cellulose nanocrystal [10] and of porous cellulose [37] gives rise to tensile strength values comparable to that of the present neat PHBH film.

3.1. Gas transport properties

The gas transport properties were analyzed in the 295–343 K interval which is below T_c and T_m . Symbols in Fig. 6 represent the $j_m(t)$ permeation curve obtained exposing the neat PHBH membrane to the four test gases at $T = 330 \pm 1$ K with $P_{HPS} = 35$ kPa: for each examined gas, the $j_m(t)$ curve shows an initial transient time interval where the permeation flux increases with time t then reaches stationary transport conditions (stc) where $j_m(t)$ assumes a constant value J_{stc} . We analyzed the experimental $j_m(t)$ curves in the framework of the solution-diffusion model which assumes that the gas permeability P of a polymer membrane is controlled by the gas diffusivity D and solubility S in the membrane layers [41]. In the present planar samples with thickness l much lower

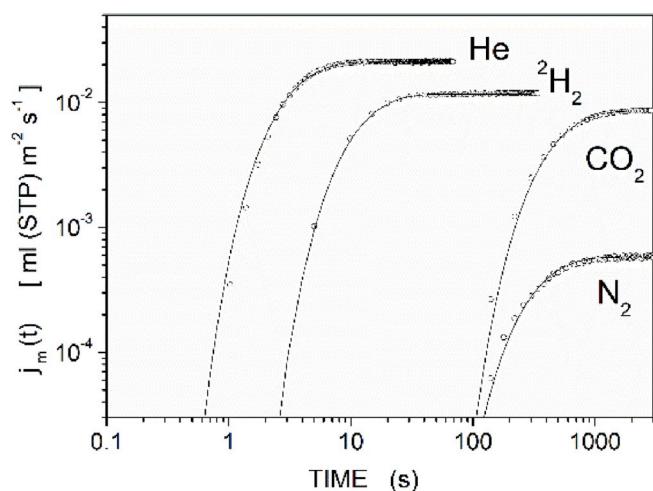


Fig. 6. Permeation curves $j_m(t)$ obtained at $T = 330 \pm 1$ K and $P_{HPS} = 35$ kPa with the 70 μm thick neat PHBH film with the examined test gases. Data are reported as open symbols while lines are the $j(t)$ curves obtained by the solution-diffusion model.

than the membrane lateral size, with the HPS exposed to the gas at pressure P_{HPS} and the LPS facing the continuously pumped analysis chamber, $P_{LPS} \sim 0$, the gas transport parameters can be evaluated fitting the experimental $j_m(t)$ flux values with the equation [42]:

$$j(t) = J_{stc} \left[1 + 2 \sum_{n \geq 1} (-1)^n \exp\left(-\frac{D n^2 \pi^2 t}{l^2}\right) \right] \quad (2)$$

where:

$$J_{stc} = \frac{P}{l} P_{HPS} \quad (3)$$

is the permeation flux in stationary transport condition; $P = D S$ is the gas permeability.

To obtain the gas permeability P and diffusivity D values as a function of temperature T , the $j_m(t)$ curves were collected in the 295 ± 1 to 343 ± 1 K temperature range. The gas permeability P was evaluated from the value of the permeation flux in stationary transport conditions using eq. (3). The penetrant diffusivity D was obtained fitting the obtained $j_m(t)$ curves with eq. (2) and the solubility value S was then evaluated by the relation $S = P/D$. The Arrhenius plots of the obtained P , D and S values for the examined test gases are reported in Fig. 7. Fitting experimental transport parameters by the equation $D = D_0 e^{-\frac{E_D}{RT}}$, $P = P_0 e^{-\frac{E_P}{RT}}$ and $S = S_0 e^{-\frac{E_S}{RT}}$ (see dashed lines) permitted to obtain the activation energy value for penetrant diffusion (E_D), permeation (E_P) and solution (E_S), see Table 2.

It was not possible to obtain the N_2 transport data at temperatures lower than $T = 303$ K because the nitrogen permeation flux was under the detection limit of our apparatus $\sim 1 \times 10^{-5}$ mL(STP) $\text{m}^{-2} \text{s}^{-1}$. A P value lower than 5×10^{-8} mL(STP) $\mu\text{m} \text{m}^{-2} \text{s}^{-1} \text{Pa}^{-1}$ can be thus estimated using the relation $\delta j_m > \frac{P}{l} P_{HPS} = J_{stc}$.

Looking at Table 2, at Fig. 7 and the physical-chemical parameters of the examined test gases it is also observed that: i) the gas diffusivity decreases increasing the size of the penetrant molecule, ii) the activation energy for diffusion increases with the size of the penetrant molecule from ~ 20 kJ/mol for He to ~ 67 kJ/mol for N_2 , iii) the gas solubility is a weakly temperature dependent quantity; its value increases with the penetrant condensation temperature.

In semi-crystalline polymer the migration of penetrant molecules occurs in the amorphous fraction of the polymer matrix as crystalline domain are effectively impermeable to the penetrant molecules or the polymer crystallites [43–45]. The present activation energy values thus describe energy barriers to the solution and migration of penetrant molecules in the amorphous fraction of the PHBH matrix.

Before going on with the discussion it's worthy to compare the values of the gas transport parameters of the present solution-casted PHBH films with permeability values of representative polymer materials, see Table 3. It can be noted that the present PHBH film acts as better gas barrier for CO_2 and N_2 that poly(lactic acid) (PLA, deeply investigated biopolymer for packaging applications) and well compare with Polyethylene Terephthalate (PET) which is a petroleum-derived polymer having commercial character. Improvements are, on the contrary, required to reach the barrier performances of Ethylene Vinyl Alcohol (EVOH).

The gas transport properties of the GO-PHBH film were studied analyzing the $j_m(t)$ curves obtained exposing a 65 μm thick nanocomposite GO-PHBH film to the test gases at $P_{HPS} = 35$ kPa. Fig. 8 reports $j_m(t)$ curves pertinent to $^2\text{H}_2$ and CO_2 penetrant molecules in the upper and lower panel respectively.

It can be observed that at each examined temperature the dispersion of GO filler nanoparticles: i) reduces the J_{stc} values with respect to those of the neat PHBH matrix and ii) produces interval times for transient transport conditions longer than those of the neat PHBH matrix.

The value of the gas transport parameters was obtained analyzing the $j_m(t)$ curves with the same procedure as with the neat PHBH films, see

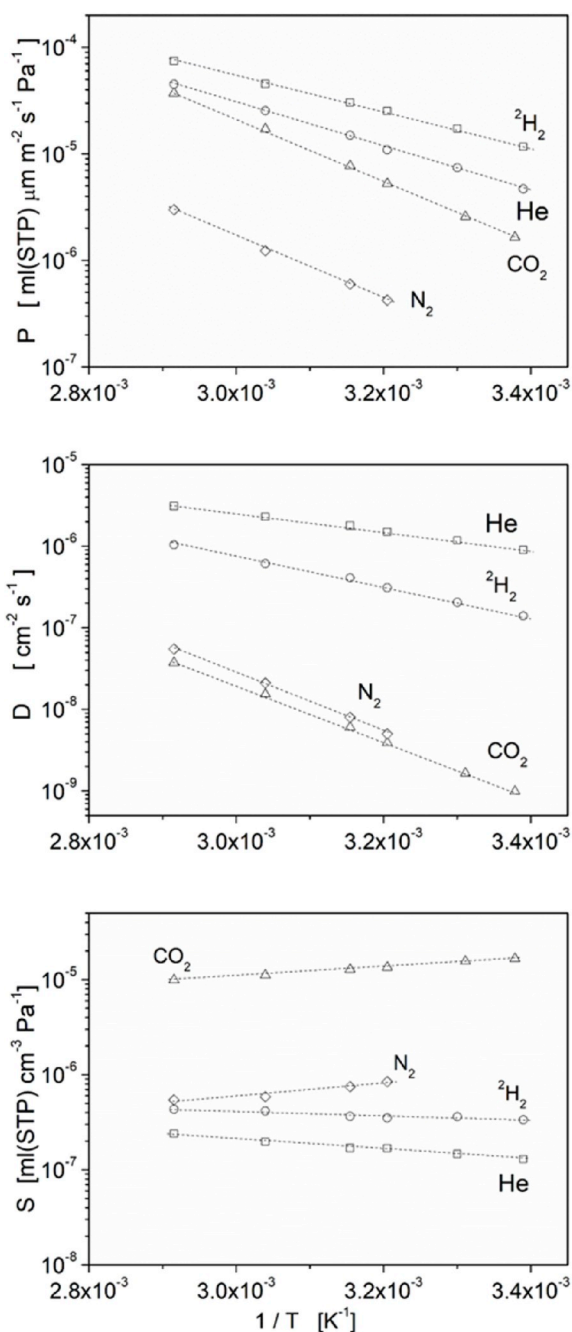


Fig. 7. Arrhenius plot of permeability (P), diffusivity (D) and solubility (S) values of the examined test gas in the neat PHBH film.

Table 2

Activation energy values for test gas permeation (E_p), diffusion (E_D) and solution (E_S) in the neat PHBH and nanocomposite GO-PHBH films.

	E_p (kJ/mol)	E_D (kJ/mol)	E_S (kJ/mol)
He	PHBH: 31.3 ± 0.8	PHBH: 21.0 ± 0.8	PHBH: 10.3 ± 0.8
	GO-PHBH: 32.3 ± 0.8	GO-PHBH: 20.9 ± 0.8	GO-PHBH: 11 ± 1
$^2\text{H}_2$	PHBH: 39.1 ± 0.8	PHBH: 34.2 ± 0.8	PHBH: 4.5 ± 0.8
	GO-PHBH: 40.7 ± 0.8	GO-PHBH: 34.9 ± 0.8	GO-PHBH: 5 ± 1
N_2	PHBH: 54.8 ± 0.8	PHBH: 67.2 ± 0.8	PHBH: (12 ± 2)
	GO-PHBH: 53 ± 2		
CO_2	PHBH: 56.0 ± 0.8	PHBH: 65.9 ± 0.8	PHBH: (10 ± 2)
	GO-PHBH: 58 ± 2	GO-PHBH: 67 ± 2	GO-PHBH: (11 ± 2)

Table 3

Gas permeability P of the present neat PHBH film (first row) and of references polymers. EVOH29, 32, 38, 44, 57 are EVOH containing 29, 32, 38, 44 ethylene mol. %. *: under the detection limit (see text). (a): fully amorphous; (b): biaxially oriented, 30% crystalline.

	CO_2 ($\frac{\text{ml}\mu\text{m}}{\text{m}^2\text{sPa}}$)	N_2 ($\frac{\text{ml}\mu\text{m}}{\text{m}^2\text{sPa}}$)	H_2 ($\frac{\text{ml}\mu\text{m}}{\text{m}^2\text{sPa}}$)
Neat PHBH; 22 °C	1.65×10^{-6}	*	4.7×10^{-6}
PLA; 35 °C [46]	1.0×10^{-5}	4.2×10^{-7}	4.8×10^{-5}
PLA; 30 °C [47]	8.3×10^{-6}	3.8×10^{-7}	
PLA; 20 °C [41]	6.1×10^{-6}	2.4×10^{-7}	2.3×10^{-5}
PET ^(a) ; 25 °C [48]	2×10^{-6}	1×10^{-6}	
PET ^(b) ; 25 °C [49]	1.1×10^{-6}	6.8×10^{-8}	
EVOH32; 23 °C [50]	1.4×10^{-9}	$\sim 10^{-10}$	6.96×10^{-8}
EVOH38; 23 °C [50]	3.0×10^{-9}	2×10^{-10}	
EVOH44; 23 °C [50]	9.6×10^{-9}		
EVOH29; 25 °C [51]	$(1 \div 2) \times 10^{-8}$	4×10^{-10}	

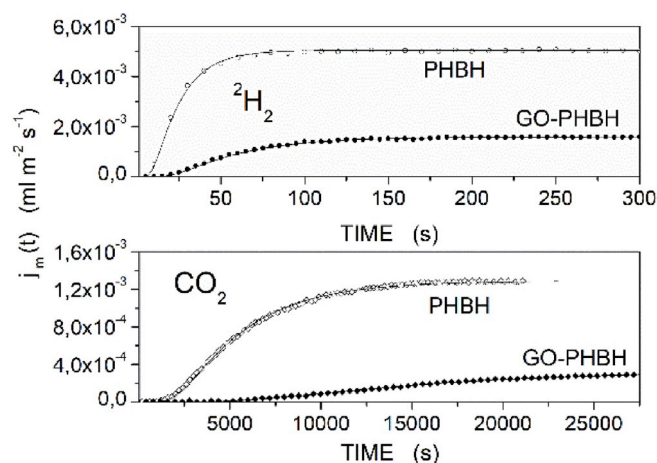


Fig. 8. Permeation curves $j_m(t)$ obtained at $T = 310 \pm 1$ K and $P_{HPS} = 35$ kPa with the neat PHBH film (open symbols) and composite GO-PHBH film (solid symbols) for $^2\text{H}_2$ (upper panel) and CO_2 (lower panel). Lines fitting the experimental data are the $j(t)$ curves obtained by the solution-diffusion model.

Fig. 9. In this Figure, symbols report the permeability (P) and diffusivity (D) values: open symbols for the neat PHBH film, solid symbols for the nanocomposite GO-PHBH film. The following symbols identify the test gases: squares for He, triangles for CO_2 , circles for $^2\text{H}_2$ and diamonds for N_2 . Data pertinent to the neat PHBH film are reported because the comparison with data pertinent to the GO-PHBH film permits to rationalize the obtained experimental results. Looking at Fig. 9 it can be, in fact, observed that the GO filler addition:

- reduces the permeability values by the same extent at each of the examined temperature. The reduction factor $r_p = \frac{P_{\text{PHBH}}}{P_{\text{GO-PHBH}}} \sim 6$ for CO_2 and N_2 and ~ 3 for $^2\text{H}_2$ and He.
- reduces the diffusivity values by the same extent at each of the examined temperature. The reduction factor $r_D = \frac{D_{\text{PHBH}}}{D_{\text{GO-PHBH}}}$ is ~ 5 for CO_2 and ~ 2 for $^2\text{H}_2$ and He, see lower panels (given the low signal-to-noise ratio, it was not possible to obtain reliable evaluations for the N_2 diffusivity in the GO-PHBH sample).

Fitting the experimental P and D data for the GO-PHBH film by Arrhenius equation provides E_D and E_p values which are coincident, inside the experimental indetermination, with those of pure PHBH sample, see Table 2.

The improved gas barrier performances of the GO-PHBH nanocomposite for all examined gas, see the r_p factor, are accompanied by a reduction of the gas diffusivity, see the r_D factor: the evidence that $r_D \sim r_p$ indicates that the permeability reduction was caused by a reduced

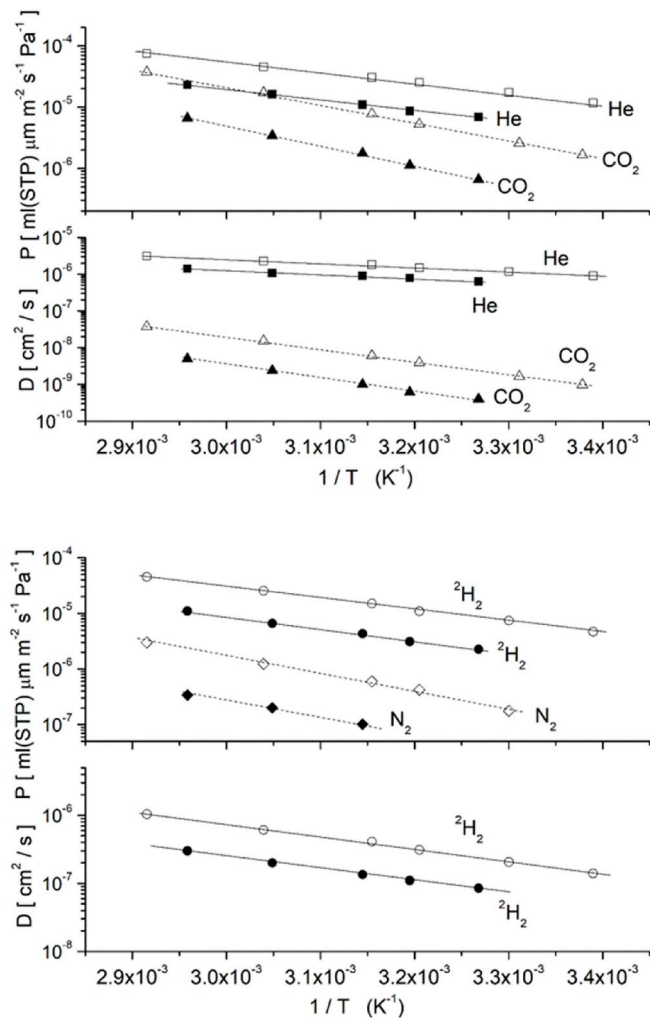


Fig. 9. Permeability (P) and diffusivity (D) values in neat PHBH films (open symbols) and in nanocomposite GO-PHBH films (solid symbols). Squares: He. Triangles: CO_2 . Circles: $^2\text{D}_2$. Diamonds: N_2 .

penetrant diffusivity. Considering that the GO filler addition does not change the free volume structure of the amorphous region of PHBH, we suggest that the reduced penetrant diffusivity arises from geometrical effects rather than by changes in the penetrant diffusion mechanism through the PHBH matrix. Table 2 shows that with each examined gas E_D values in the neat PHBH film are equivalent to those of GO-PHBH: this evidence strongly supports the previous suggestion.

A possible explanation for the diffusivity reduction in the present nanocomposite is the fact that the GO gas-impermeable domains force permeating penetrant molecules to overcome them migrating along diffusive paths with average length $l = \tau h$ where h is the membrane thickness and τ is the so-called tortuosity factor. The apparent gas diffusivity in the nanocomposite, D_{NC} , decreases according to the relation $D_{NC} = \frac{D_M}{\tau}$ where D_M is the gas diffusivity in the pure matrix; τ can be evaluated by the relation $\tau = 1 + \frac{w}{2t}\phi_c$ where w and t are the average size and thickness of the impermeable GO domains and ϕ_c is the volume fraction of the gas impermeable domains in the nanocomposite [52]. Note that this evaluation of the tortuosity factor assumes that the GO filler particles are well stacked with their surface normal to the flux direction. These domains also reduce the apparent gas solubility of the nanocomposite by the relation $S_{NC} = S_M(1 - \phi_c)$ where S_M is the gas solubility in the pure matrix. The following equation holds for the nanocomposite permeability P_{NC} :

$$P_{NC} = D_{NC}S_{NC} = \frac{D_M S_M}{\tau} (1 - \phi_c) = P_M \left(\frac{1 - \phi_c}{1 + \frac{w}{2t}\phi_c} \right) \quad (4)$$

where $P_M = D_M S_M$ is the permeability of the pure matrix [52].

Let us evaluate the contribution of the filler particles to the nanocomposite gas barrier properties considering that $w \sim 10 \mu\text{m}$ (according to the producer's specifications), $\phi_c^{GO} \sim 0.25 \text{ vol } \%$ (this is a lower extremal value for ϕ_c^{GO} evaluated assuming that the GO mass density is the same as that of PHBH) and $t \sim 1 \text{ nm}$ [53,54]. Then $(1 - \phi_c) \sim 1$ and $\tau > 40$ which indicates that expected r_p values are much larger than experimentally observed: this suggests that GO filler particles dispersed in the PHBH matrix are randomly oriented and don't limit the penetrant transport rates.

In order to understand the diffusivity reduction mechanism it's necessary to remark the key information provided by the structural analysis of the neat PHBH and nanocomposite GO-PHBH films. The neat PHBH samples have semi-crystalline structure with crystalline volume fraction $x_c^{PHBH} \sim 0.28$; the crystalline domains are in form of randomly oriented spherulites with average size $d_c = 5 \pm 1 \text{ nm}$ and $d_b = 30 \pm 1 \text{ nm}$ in the c - and b -axis direction, respectively. The free volume of the amorphous PHBH matrix consists of cavities with average radius $r_c = 0.29 \pm 0.01 \text{ nm}$ where all penetrant molecules can be thus accommodated ($\sigma_k < 2 r_c$). In the nanocomposite samples the PHBH crystalline fraction was larger than in the neat film increasing to $x_c^{GO-PHBH} \sim 0.60$ without relevant variations in the PHBH crystallite size (d_b grows to $36 \pm 1 \text{ nm}$); negligible changes also occurs in the free volume structure of the nanocomposite matrix.

It can be suggested that the improved gas barrier properties after GO addition are attributable to the increased crystalline fraction of the PHBH matrix, see Table 1, which occurs acting the GO particles as heterogeneous sites for the nucleation of PHBH crystallites.

Let us now evaluate the r_p factor as predicted by eq. (4) adapting the parameters describing the geometry of the filler particle to the geometry of the PHBH nano-crystalline domains (as revealed by the XRD analysis) and considering the crystalline fraction of the neat and nanocomposite film samples (as revealed by DSC analysis):

- a The crystalline domains are spherulites randomly oriented with respect to the direction of the permeation flux direction; then $\frac{w}{2t} = \frac{1}{2}$ and the tortuosity factor reduces to $\tau = 1 + \frac{1}{2}\phi_c$.
- b The filler volumetric fraction is the volumetric fraction of the crystalline PHBH phase as the GO filler contribution can be neglected as $\phi_c^{GO} \ll x_c$. Consequently in the neat PHBH films $\phi_c = x_c^{PHBH} = 0.28$ while in the nanocomposite GO-PHBH film $\phi_c = x_c^{GO-PHBH} = 0.60$.

Let us define P_{PHBH}^0 as the gas permeability of the neat PHBH matrix when completely amorphous. Then according to eq. (4), the permeability of the neat PHBH film, P_{PHBH} , is given by $P_{PHBH} =$

$$P_{PHBH}^0 \left(\frac{1 - x_c^{PHBH}}{1 + \frac{1}{2}x_c^{PHBH}} \right) \text{ while that of the GO-PHBH nanocomposite film,}$$

$$P_{GO-PHBH} \text{ is given by } P_{GO-PHBH} = P_{PHBH}^0 \left(\frac{1 - x_c^{GO-PHBH}}{1 + \frac{1}{2}x_c^{GO-PHBH}} \right). \text{ The value of the}$$

$$r_p = \frac{P_{PHBH}}{P_{GO-PHBH}} = \frac{\frac{1 - x_c^{GO-PHBH}}{1 + \frac{1}{2}x_c^{GO-PHBH}}}{\frac{1 - x_c^{PHBH}}{1 + \frac{1}{2}x_c^{PHBH}}} \text{ factor is } \sim 2 \text{ consistent with experimental data}$$

pertinent to the small-size penetrants but under-estimating data pertinent to the large-size ones. Note that r_p data for CO_2 and N_2 could be

reproduced with $x_c^{GO-PHBH} = 80$ vol %: reasonably this “apparent” larger than experimentally obtained crystalline fraction can be explained by the presence of regions in the PHBH amorphous matrix where the reduced mobility of the PHBH chains gives rise to lower local permeability values for the large size molecules, as for example, the regions between crystalline domains or the onset of dead-end channels between the PHBH crystallites [55].

The r_p factor was also calculated in the framework of other models for gas permeability of nanocomposite membranes, modelling the neat and nanocomposite PHBH films as consisting of an amorphous, gas-permeable PHBH matrix with dispersed gas-impermeable PHBH crystalline domains [56–62]. Calculation provide r_p values ~ 2 as using Nielsen eq. (4).

4. Conclusions

Pure PHBH films and nanocomposite GO-PHBH films with 0.25 wt % filler particles were prepared by solution-casting method. The addition of this small additive quantity introduces negligible variation of the PHBH melting temperature $T_m \sim 135$ °C and free volume structure but increases the PHBH crystalline fraction x_c from 0.28 to 0.60 acting the GO particles as preferential nucleation site for the PHBH crystallites. The PHBH crystalline domains consisted of nano-sized spherulites with same shape both in the neat and nanocomposite samples. The presence of GO produced a makeable improvement of the PHBH gas barrier properties. In fact, in the 296–343 K temperature range, the gas permeability decreased by a factor 2 for He and $^2\text{H}_2$ and by a factor 6 for CO_2 and N_2 with respect to that of the neat PHBH film. Gas transport was controlled by the solution-diffusion mechanism and the permeability decrease in the nanocomposite was a consequence of the increased number density of the gas impermeable PHBH crystalline spherulites forcing penetrant molecules to migrate along longer diffusive paths. The obtained gas permeability values of the neat PHBH films and the improved gas barrier properties of the nanocomposite films indicate that PHBH-based nanocomposites can be proposed as biopolymer gas barrier films.

Author contributions

The manuscript was written through contributions of all authors. All authors have given their approval to the final version of the manuscript. All authors contributed equally.

Declaration of competing interest

The authors declare no competing financial interest.

Appendix A. Supplementary data

Supplementary data to this article can be found online at <https://doi.org/10.1016/j.polymertesting.2019.106181>.

References

- [1] Y. Doi, *Microbial Polyesters*, VCH Publishers, New York, 1990.
- [2] M. Biron, *Industrial Applications of Renewable Plastics*, Elsevier, Amsterdam, 2017.
- [3] Y. Doi, S. Kitamura, H. Abe, *Microbial synthesis and characterization of poly(3-hydroxybutyrate-co-3-hydroxyhexanoate)*, *Macromolecules* 28 (1995) 4822–4828.
- [4] Y. Xie, D. Kohls, I. Noda, D.W. Schaefer, Y.A. Akpalu, *Poly(3-hydroxybutyrate-co-3-hydroxyhexanoate) nanocomposites with optimal mechanical properties*, *Polymer* 50 (2009) 4656–4670.
- [5] S.K. Misra, S.P. Valappil, I. Roy, A.R. Boccaccini, *Polyhydroxyalkanoate (PHA)/inorganic phase composites for tissue engineering applications*, *Biomacromolecules* 7 (2006) 2249–2258.
- [6] A.K. Mohanty, M. Misra, G. Biofibers Hinrichsen, *Biodegradable polymers and biocomposites: an overview*, *Macromol. Mater. Eng.* 276/277 (2000) 1–24.
- [7] Yi Yang, Shanming Ke, Ren Li, Yingjun Wang, Yiyang Li, *Dielectric spectroscopy of biodegradable poly(3-hydroxybutyrate-co-3-hydroxyhexanoate) films*, *Eur. Polym. J.* 48 (2012) 79–85.
- [8] Q. Liao, I. Noda, C.W. Frank, *Melt viscoelasticity of biodegradable poly(3-hydroxybutyrate-co-3-hydroxyhexanoate) copolymers*, *Polymer* 50 (2009) 6139–6148.
- [9] M. Niaounakis, *Biopolymers: Applications and Trends*, Elsevier, Oxford, 2015, p. 18.
- [10] J. Zhou, X. Ma, J. Li, L. Zhu, *Preparation and characterization of a bio-nanocomposite from poly(3-hydroxybutyrate-co-3-hydroxyhexanoate) and cellulose nanocrystals*, *Cellulose* 26 (2019) 979–990.
- [11] P. Xu, Y. Cao, B. Wu, P. Ma, W. Dong, H. Bai, H. Zhang, H. Zhu, M. Chen, *Effect of modified nanocrystalline cellulose on the hydrophilicity, crystallization and mechanical behaviour of poly(3-hydroxybutyrate-co-3-hydroxyhexanoate)*, *New J. Chem.* 42 (2018) 11972–11978.
- [12] W. Arifin, T. Kuboki, *Effect of glass fibers on mechanical and thermal properties of poly(3-hydroxybutyrate-co-3-hydroxyhexanoate)*, *Polym. Compos.* 39 (2018) 491–503.
- [13] J.R. Potts, D.R. Dreyer, C.W. Bielawski, R.S. Ruoff, *Graphene-based polymer nanocomposites*, *Polymer* 52 (2011) 5–25.
- [14] H. Kim, A.A. Abdala, C.W. Macosko, *Graphene/polymer nanocomposites*, *Macromolecules* 43 (2010) 6515–6530.
- [15] B.A. Morris, *The Science and Technology of Flexible Packaging*, Elsevier, Amsterdam, 2017.
- [16] I.J. Church, A.L. Parsons, *Modified atmosphere packaging technology: a review*, *J. Sci. Food Agric.* 67 (1995) 143–152.
- [17] O.J. Caleb, U.L. Opara, P.V. Mahajan, F.A.J. Al-Said, *Modified atmosphere packaging technology of fresh and fresh-cut produce and the microbial consequences-A review*, *Food Bioprocess Technol.* 6 (2013) 303–329.
- [18] C.A. Mireles, M. DeWitt, A.C.M. Oliveira, *Modified atmosphere systems and shelf life extension of fish and fishery products*, *Foods* 5 (2016) 48.
- [19] D. Feldman, *Polymer nanocomposite barriers*, *J. Macromol. Sci., Pure Appl. Chem.* 50 (2013) 441–448.
- [20] D. Feldman, *Polymer barrier films*, *J. Polym. Environ.* 9 (2001) 49–55.
- [21] X. Lefebvre, D. Pasquier, S. Gonzalez, T. Epszstein, M. Chirat, F. Demanze, *Development of reactive barrier polymer against corrosion for the oil and gas industry*, *Oil Gas Sci. Technol.* 70 (2015) 291–303.
- [22] T.P. Raine, O.M. Istrate, B.E. King, B. Craster, I.A. Kinloch, P.M. Budd, *Graphene/polyamide laminates for supercritical CO₂ and H₂S barrier applications: an approach toward permeation shutdown*, *Adv. Mater. Interfaces* 5 (2018), 1800304.
- [23] K. Gaska, R. Kadar, A. Rybak, A. Siwek, S. Gubanski, *Gas barrier, thermal, mechanical and rheological properties of highly aligned graphene-LDPE nanocomposites*, *Polymers* 9 (2017) 294.
- [24] R. Krause-Rehberg, H.S. Leipner, *Positron Annihilation in Semiconductors: Defect Studies*, Springer-Verlag GmbH & Co. KG, Berlin and Heidelberg, Germany, 2010. <http://prac.us.edu.pl/~kansy/index.php?id=itpolym>.
- [25] P.A. Redhead, J.P. Hobson, E.V. Kornelsen, *The Physical Basis of Ultrahigh Vacuum*, American Institute of Physics, New York, 1993, p. 15.
- [26] D. Roilo, C.A. Maestri, M. Scarpa, P. Bettotti, W. Egger, T. Koschine, R.S. Brusa, R. Checchetto, *Cellulose nanofibrils films: molecular diffusion through elongated sub-nano cavities*, *J. Phys. Chem. C* 121 (2017) 15347–15447.
- [27] R. Checchetto, P. Bettotti, R.S. Brusa, G. Carotenuto, W. Egger, C. Hugenschmidt, A. Miotello, *Anomalous molecular infiltration in graphene laminates*, *Phys. Chem. Chem. Phys.* 20 (2018) 24671–24680.
- [28] C. Ding, B. Chen, Q. Wu, *DSC analysis of isothermally melt-crystallized bacterial poly(3-hydroxybutyrate-co-3-hydroxyhexanoate) films*, *J. Therm. Anal. Calorim.* 103 (2010) 1001–1006.
- [29] P. Pan, Z. Liang, N. Nakamura, T. Miyagawa, Y. Inoue, *Uracil as nucleating agent for bacterial poly[(3-Hydroxybutyrate)-co-(3-hydroxyhexanoate)] copolymers*, *Macromol. Biosci.* 9 (2009) 585–595.
- [30] H. Wang, K. Tashiro, *Reinvestigation of crystal structure and intermolecular interactions of biodegradable poly(3-hydroxybutyrate) α -form and the prediction of its mechanical properties*, *Macromolecules* 49 (2016) 581–594.
- [31] C. Liu, I. Noda, D.C. Martin, B.D. Chase, C. Ni, J.F. Rabolt, *Growth of anisotropic single crystals of a random copolymer, poly[(R)-3-hydroxybutyrate-co-(R)-3-hydroxyhexanoate] driven by cooperative -CH \cdots O H-bonding*, *Polymer* 154 (2018) 111–118.
- [32] H. Abe, Y. Doi, H. Aoki, T. Akehata, *Solid-state structures and enzymatic degradabilities for melt-crystallized films of copolymers of (R)-3-Hydroxybutyric acid with different hydroxyalkanoic acid*, *Macromolecules* 31 (1988) 1791–1797.
- [33] S.K. Shamar, P.K. Pujari, *Role of free volume characteristics of polymer matrix in bulk physical properties of polymer nanocomposites: a review of positron annihilation lifetime studies*, *Prog. Polym. Sci.* 75 (2017) 31–47.
- [34] S.J. Tao, *Positronium annihilation in molecular substances*, *J. Chem. Phys.* 56 (1972) 5499–5510.
- [35] M. Eldrup, D. Lightbody, J.N. Sherwood, *The temperature dependence of positron lifetimes in solid pivalic acid*, *Chem. Phys.* 58 (1981) 51–58.
- [36] N. Hosoda, T. Tsujimoto, H. Uyama, *Green composites of Poly(3-hydroxybutyrate-co-3-hydroxyhexanoate) reinforced with porous cellulose*, *ACS Sustain. Chem. Eng.* 2 (2014) 248–253.
- [37] D.R. Paul, L.M. Robeson, *Polymer nanotechnology: nanocomposites*, *Polymer* 49 (2008) 3187–3204.
- [38] A.F. Ismail, G.P. Sean, K.C. Wong, P.S. Goh, A.F. Ismail, in: *Carbon-Based Polymer Nanocomposites for Environmental and Energy Applications*, Elsevier, Amsterdam, 2018, pp. 233–260. Chapt. 10: Carbon-Based Nanocomposite Membrane for Acid Gas Separation.
- [39] P.K. Tewari, *Nanocomposite Membrane Technology, Fundamentals and Applications*, CRC Press, Boca Raton, 2016, pp. 263–280. Chapt. 7, Challenges in processing of nanocomposites membranes.

- [41] Y. Yampolskii, I. Pinneau, B. Freeman, *Materials Science of Membranes for Gas and Vapor Separation*, John Wiley & Sons, Ltd, Chichester, West Sussex, 2006.
- [42] J. Crank, *The Mathematics of Diffusion*, Clarendon Press, Oxford, 1979.
- [43] A.S. Michaels, H.J. Bixler, H.L. Fun, Gas transport properties in thermally conditioned liner polyethylene, *J. Appl. Phys.* 35 (1964) 3165–3178.
- [44] M. Drieskens, R. Peeters, J. Mullens, D. Franco, P.J. Lemstra, D.G. Hristova-Bogaerds, Structure versus properties relationship of poly(lactic acid). I. Effect of crystallinity on barrier properties, *J. Polym. Sci., Part B: Polym. Phys.* 47 (2009) 2247–2258.
- [45] M. Cocca, M.L. Di Lorenzo, M. Malinconico, V. Frezza, Influence of crystal polymorphism on mechanical and barrier properties of poly(lactic acid), *Eur. Polym. J.* 47 (2011) 1073–1080.
- [46] T. Komatsuka, A. Kusakabe, K. Nagai, Characterization and gas transport properties of poly(lactic acid) blend membranes, *Desalination* 234 (2008) 212–220.
- [47] L. Bao, J.R. Dorgan, D. Knauss, S. Hait, N.S. Oliveira, I.M. Marrucho, Gas permeation properties of poly(lactic acid) revisited, *J. Membr. Sci.* 285 (2006) 166–172.
- [48] A.S. Michaels, A.S. Vieth, J.A. Barrie, Diffusion of gases in poly(ethylene terephthalate), *J. Appl. Phys.* 34 (1963) 13–20.
- [49] E.A. McGonigle, J.J. Liggat, R.A. Pethrick, S.D. Jenkins, J.H. Daly, D. Haywar, Permeability of N₂, Ar, He, O₂ and CO₂ through biaxially oriented polyester films – dependence on free volume, *Polymer* 42 (2001) 2413–2426.
- [50] C. Maes, W. Luyten, G. Herremans, R. Peeters, R. Carleer, M. Buntink, Recent updates on the barrier properties of ethylene vinyl alcohol copolymer (EVOH): a review, *Polym. Rev.* 58 (2018) 209–246.
- [51] J.A. Soto Puente, K. Fatyeyeva, C. Chappev, S. Marais, E. dargent, Layered poly(ethylene-co-vinyl acetate)/Poly(ethylene-co-vinyl alcohol) membranes with enhanced water separation selectivity and performances, *ACS Appl. Mater. Interfaces* 9 (2017) 6411–6423.
- [52] L.E. Nielsen, Models for the permeability of filled polymer systems, *J. Macromol. Sci. Part A – Chemistry* 1 (1967) 929–942.
- [53] I. Jung, M. Vaupel, M. Pelton, R. Piner, D.A. Dikin, S. Stankovich, J. An, R.S. J. Ruoff, Characterization of thermally reduced graphene oxide by imaging ellipsometry, *Phys. Chem. C* 112 (2008) 8499–8506.
- [54] Z. Luo, Y. Lu, L.A. Somers, A.T.C. Johnson, High yield preparation of macroscopic graphene oxide membranes, *J. Am. Chem. Soc.* 131 (2009) 898–899.
- [55] D. Roilo, P.N. Patil, R.S. Brusa, A. Miotello, S. Aghion, R. Ferragut, R. Checchetto, Polymer rigidification in graphene based nanocomposites: gas barrier effects and free volume reduction, *Polymer* 121 (2017) 17–25.
- [56] J.C.A. Maxwell, *Treatise on Electricity and Magnetism*, Dover Publications, New York, 1954.
- [57] D.A.G. Bruggeman, Berechnung verschiedener physikalischer Konstanten von heterogenen Substanzen, *Ann. Phys.* 24 (1935) 636–664.
- [58] J. Petropoulos, A comparative study of approaches applied to the permeability of binary composite polymeric materials, *J. Polym. Sci. Polym. Phys. Ed* 23 (1985) 1309–1324.
- [59] L.G. Toy, B.D. Freeman, R.J. Spontak, A. Morisato, I. Pinneau, Gas permeability and phase morphology of Poly(1-(trimethylsilyl)-1-propyne)/Poly(1-phenyl-1-propyne) Blends, *Macromolecules* 30 (1997) 4766–4769.
- [60] T. Lewis, L. Nielsen, Dynamic mechanical properties of particulate- filled composites, *J. Appl. Polym. Sci.* 14 (1970) 1449–1471.
- [61] L. Nielsen, Thermal conductivity of particulate- filled polymers, *J. Appl. Polym. Sci.* 17 (1973) 3819–3820.
- [62] R. Pal, Permeation models for mixed matrix membranes, *J. Colloid Interface Sci.* 317 (2008) 191–198.